Axial Atmospheric Angular Momentum Budget at Diurnal and Sub-Diurnal Periodicities

François Lott[1], Olivier de Viron[2], Pedro Viterbo [3] [4], and François Vial[5]

April 23, 2007

Abstract

The diurnal and sub-diurnal variations of the mass and wind terms of the axial Atmospheric Angular Momentum (AAM) are explored using a 1-year integration of the LMDz-GCM, twelve 10-day ECMWF forecasts and some ECMWF Analysis products. In these datasets, the wind and mass AAMs present diurnal and semi-diurnal oscillations which tendencies far exceed the total torque.

In the LMDz-GCM, these diurnal and semi-diurnal oscillations are associated with axisymmetric ($s = 0$) and barotropic circulation modes that resemble to the second gravest ($n = 2$) Eigensolution of the Laplace's tidal equations. This mode induces a Coriolis conversion from the wind AAM toward the mass AAM that far exceeds the total torque. At the semi-diurnal period, this mode dominates the axisymmetric and barotropic circulation. At the diurnal period, this $n = 2$ mode is also present, but the barotropic circulation also presents a mode resembling to the first gravest ($n = 1$) Eigensolution of the tidal equations. This last mode does not produce anomalies in the mass and wind AAMs.

A shallow water axisymmetric model driven by zonal mean zonal forces which vertical integral equal the zonal mean zonal stresses issued from the GCM is then used to interpret these results. This model reproduces well the semi diurnal oscillations in mass and wind AAMs, and the semi-diurnal mode resembling to the $n = 2$ Eigensolution that produces them, when the forcing is distributed barotropically in the vertical direction. This model also reproduces diurnal modes resembling to the $n = 1$ and $n = 2$ Eigensolutions when the forcings are distributed more baroclinically. Among the dynamical forcings that produce these modes of motion, we found that the mountain forcing and the divergence of the AAM flux are equally important, and more efficient than the boundary layer friction.

In geodesy, the large but opposite signals in the mass and wind AAMs due to the $n = 2$ modes can lead to large errors in the evaluation of the AAM budget. The $n = 2$ responses in surface pressure can affect the Earth Ellipcity, and the $n = 1$ diurnal response can affect the geocenter position. For the surface pressure tide, our results suggest that the dynamical forcings of the zonal mean zonal flow are a potential cause for its $s = 0$-component.

---

[1]Corresponding author address: Dr François Lott, LMD/IPSL CNRS, Ecole Normale Supérieure, 24 rue Lhomond, 75231 PARIS Cédex 05, France. Phone: 33 (0)1 44 32 27 52; Fax: 33 (0)1 43 36 83 92; E-mail: flott@lmd.ens.fr

[2]Institut de Physique du Globe, Paris, France

[3]European Center for Medium-Range Weather Forecasts, Reading, England

[4]Current affiliation: Instituto de Meteorologia/Instituto D. Luìs, Lisboa, Portugal

[5]LMD/IPSL CNRS, Ecole Polytechnique, Palaiseau, France

1   Introduction

Over the last 4 decades, the budget of Atmospheric Angular Momentum (AAM) has been the subject of many studies. For the geodesists, this interest follows that at near all periodicities, changes in AAM correspond to changes in the parameters of the Earth rotation (Barnes et al. 1983). For the climatologists, this interest follows that the AAM varies with the planetary scale tropical oscillations affecting the climate at intra-seasonal (Madden 1987, Hendon 1995) and inter-annual (Chao 1989) time scales. In the extratropics, and at shorter time scales, it also varies with traveling Rossby waves (Lejenas and Madden 2000), low-frequency oscillations (Lott et al. 2001, 2004a), weather regimes (Lott et al. 2004b) and synoptic scale eddies (Iskenderian and Salstein 1998).

Although early papers revealed substantial links between observed changes in AAM and the changes in the frictional torque associated with the large scale variability of the deep convection in the tropics (Madden 1987), it is now clear that at periodicities below 40-days the mountain torque dominates the friction torque. Although the relative importance of those two torques has been debated during the 1990's (see for instance Weickmann et al. 1997) less attention has been paid to the relative importance of the mass angular momentum and of the wind angular momentum in the total angular momentum itself. This follows from the fact that the mass AAM contributes little to the total AAM at long periods, where most of the AAM variance is contained. Nevertheless, at periodicities below 25-days, the variations in mass AAM compare with those in wind AAM. This equi-partition occurs because in this frequency band: (i) the total torque is dominated by the mountain torque; (ii) the major mountain ranges are located in the midlatitudes so the mountain torque is essentially due to a mountain stress applied to the atmosphere in the midlatitudes; and (iii) the atmospheric response to this stress is in geostrophic balance (see Lott and d'Andrea 2005). This process results in lead-lag relationships between the mountain torque and the mass AAM which have some interest for the low-frequency variability in the Northern Hemisphere extratropics (Lott et al. 2004a). Indeed, the leading mode of variability there, the Arctic Oscillation (Thomson and Wallace 1998), corresponds to a redistribution of mass from the polar latitudes to the midlatitudes and the subtropics. Its variations are associated with substantial changes in mass AAM (von Storch 1999, von Storch 2001). Note nevertheless that Lott and d'Andrea (2005) do not discuss the fact that the mountains stress can be transmitted to the zonal flow at a long distance from the mountains that produce it.

To interpret dynamically the partition between the mass and the wind AAM in the NCEP re-analysis data, Lott and d'Andrea (2005) also used an axisymmetric shallow water model and analyzed its balanced response. Incidently, they also found that when the mountain torque varies abruptly (i.e. with a time scale near one day), and results in a force applied to the atmosphere in the midlatitudes, it produces wind and mass AAM oscillations with periods between 12h and 24h. These oscillations are related to global scale free inertio-gravity modes with zero zonal wavenumber ($s = 0$, Longuet-Higgins 1968, hereafter LH68, Tanaka and Kasahara 1992) produced in the midlatitudes during the geostrophic adjustment of the model to the torque. Note that Egger (2003), also discussed the global adjustment to a mountain forcing in the context of the AAM budget.

In the real atmosphere, these modes can influence the AAM budget at diurnal and sub-diurnal periodicities. Indeed, as the surface pressure fields associated with the traveling atmospheric tides vary in longitude, they result in a zonal mean surface stress when the zonal pressure gradients are pronounced over the major mountain ranges. Note that this pressure

gradients can also be enhanced locally through a dynamical interaction between the traveling tidal signals and the mountains (Frei and Davies 1993). The daily cycle of the zonal mean zonal forces on the atmosphere resulting from these interactions between the traveling tides and the mountains, can trigger secondary tides with zero zonal wavenumber that give substantial but largely compensating daily fluctuations of the wind and mass AAMs.

These issues have two potential applications. The first concerns the evaluation of the Earth Orientation Parameters. Today, the major technical problems in this context are in closing the AAM budget at the daily time-scales (de Viron et al. 2005): the presence of the large canceling terms presented in this paper is probably at the origin of these problems. The second concerns the dynamics of the atmospheric tides. Indeed, our interpretation of the mass and wind AAM oscillations involve tidal modes generated by dynamical forcings which have not been studied before.

The first objective of this paper is to point out that the mass and wind terms of the axial AAM budget present daily oscillations that have no substantial impact on the total AAM itself. The second objective is to describe the zonal mean and barotropic tidal patterns associated with these oscillations. The third objective is to show that these daily oscillations are in part forced by the daily cycle of the zonal forces acting on the atmosphere.

The plan of the paper is as follows. Section 2 presents the LMDz General Circulation Model (LMDz-GCM) used, some diagnostic equations for the zonal mean and barotropic flow evolution, the AAM budget in the LMDz-GCM, and the evolutions of the mass and wind AAMs in the LMDz-GCM as well in the ECMWF forecasts and analysis. Section 3 describes the zonal mean and barotropic flow fields associated with the semi-diurnal and the diurnal motion in the LMDz-GCM. Their structure is compared to the gravest axisymmetric Eigensolutions of the Laplace's tidal equations presented in LH68. The dynamical relationship between these fields and the semi-diurnal and diurnal variations of the mass and wind AAM is also presented. Section 4 proposes a dynamical interpretation for the origin of these planetary scale modes of motion, and for the the oscillations between the mass and wind AAM. It is based on a shallow-water axisymmetric model driven by zonal forces which vertical integral equal the various stresses issued from the GCM. Section 5 summarizes and discusses the significance of our results for geodesy and for the atmospheric tides.

2   AAM budget in general circulation models

2.1   Description of the LMDz-GCM simulations

The model data are derived from a 15 months simulation done with the LMDz-GCM at 2.5^ox2.5^o horizontal resolution. The model has 19 vertical levels with a near uniform 2km resolution in the middle troposphere and up to $z = 21$km. The resolution rapidly degrades aloft, and the model has only four levels between 25km and 40km (the model top). At the lower boundary, the model is forced by Sea-Surface Temperature and Sea-Ice cover that varies along a climatological annual cycle deduced from monthly mean data. The solar short wave forcing of the model takes into account the annual cycle and the daily cycle. For a more complete description of the LMDz-GCM, see Hourdin et al. (2006) and Lott et al. (2005a).

The simulation starts from initial fields interpolated from the ECMWF re-analysis. To avoid spin-up problems, we use only the last 12 months (i.e., 1 model year beginning the 1^{rst} January). During this year, instantaneous values of the 2 dimensional fields of the surface pressure P_s, of the barotropic winds, of the meridional flux of zonal momentum, and of the subgrid scale

surface stresses are stored every 30min. Finally, it is important to recall that the LMDz-GCM closes very well the AAM budget (Lott et al. 2005b, deViron et al.2005), and has realistic tides (for the surface pressure P_s and for the barotropic winds, see deViron et al. 2005).

2.2 Zonal mean and AAM budget equations

The conservation law for the axial AAM can be derived by successive spatial integrations of the local laws for the evolution of the zonal wind and density. If we first limit these integrations to a vertical and to a zonal average we obtain:

$$\frac{\partial \mathcal{U}}{\partial t} - 2\Omega \sin \phi \mathcal{V} = \mathcal{T} + \mathcal{F} + \mathcal{B}, \tag{1}$$

$$\frac{\partial \mathcal{M}}{\partial t} + \frac{1}{r \cos \phi} \frac{\partial}{\partial \phi} \cos \phi \mathcal{V} = 0. \tag{2}$$

Here Ω is the Earth rate of rotation, ϕ is the latitude, and r is the Earth radius. In Eqs. 1–2 $\mathcal{M}$ is the zonal mean of the atmospheric mass per unit area, while $\mathcal{U}$ and $\mathcal{V}$ are the the zonal mean of the barotropic zonal and meridional momentum per unit area respectively:

$$\mathcal{M} = \frac{1}{2\pi} \int_0^{2\pi} \frac{P_s}{g} d\lambda \;,\; \mathcal{U} = \frac{1}{2\pi} \int_0^{2\pi} \int_0^{P_S} u \frac{dp}{g} d\lambda \text{ and } \mathcal{V} = \frac{1}{2\pi} \int_0^{2\pi} \int_0^{P_S} v \frac{dp}{g} d\lambda. \tag{3}$$

Here, p is the pressure, g is the gravity constant, λ is the longitude, u is the zonal wind and v is the meridional wind. The forcing terms $\mathcal{F}$, $\mathcal{B}$, and $\mathcal{T}$ in Eq. 1 are given by,

$$\mathcal{F} = -\frac{1}{r \cos^2 \phi} \frac{\partial}{\partial \phi} \frac{\cos^2 \phi}{2\pi} \int_0^{2\pi} \int_0^{P_S} uv \frac{dp}{g} d\lambda, \quad \mathcal{B} = \frac{1}{2\pi} \int_0^{2\pi} \tau_B d\lambda,$$

$$\text{and} \quad \mathcal{T} = -\frac{1}{2\pi} \frac{1}{r \cos \phi} \int_0^{2\pi} P_s \frac{\partial Z_s}{\partial \lambda} d\lambda, \quad \text{respectively.} \tag{4}$$

Here, Z_s is the altitude of the ground and τ_B is the subgrid-scale surface friction. More specifically, these forcings are the divergence of the angular momentum flux ($\mathcal{F}$), the surface stress associated with the explicit longitudinal pressure differences across mountains ($\mathcal{T}$), and the zonal mean of the parametrized surface stresses ($\mathcal{B}$). In this formalism, the global AAM tendency is given by,

$$\frac{dM}{dt} = T, \text{ where } M = M_O + M_R, \text{ and } T = T_M + T_B. \tag{5}$$

Here M is the absolute AAM, M_O is the mass AAM and M_R is the wind AAM:

$$M_O = 2\pi r^4 \Omega \int_{-\pi/2}^{\pi/2} \cos^3 \phi \, \mathcal{M} \, d\phi \;,\quad M_R = 2\pi r^3 \int_{-\pi/2}^{\pi/2} \cos^2 \phi \, \mathcal{U} \, d\phi. \tag{6}$$

Still in Eq 5, T is the total torque, T_M is the mountain torque, and T_B is the frictional torque:

$$T_M = 2\pi r^3 \int_{-\pi/2}^{\pi/2} \cos^2 \phi \, \mathcal{T} \, d\phi \;,\quad T_B = 2\pi r^3 \int_{-\pi/2}^{\pi/2} \cos^2 \phi \, \mathcal{B} \, d\phi. \tag{7}$$

To interpret the exchanges between M_R and M_O, it is also useful to split the AAM budget in Eq 5 in two parts (von Storch 2001), and to introduce the Coriolis conversion term C:

$$\frac{dM_O}{dt} = C \;,\quad \frac{dM_R}{dt} = -C + T \;, \text{ where } C = -4\pi r^3 \Omega \int_{-\pi/2}^{\pi/2} \cos^2 \phi \sin \phi \, \mathcal{V} \, d\phi. \tag{8}$$

3

2.3 AAM budget from the LMDz-GCM and the ECMWF model

An example of the evolution of the AAM in the LMDz-GCM is shown in the Fig. 1a. We see that the absolute AAM M expressed in Hadleys day (1Hd=$8.64\,10^{22}$kg m^{2}s^{-1}) has a diurnal cycle which is hardly visible. On the contrary, M_O and M_r present daily fluctuations reaching 10Hd (from minima to maxima), that nearly exactly balance to give a small daily cycle in M.

The corresponding tendencies of M, M_R, and M_O, are shown in Fig. 1b which compares them to the total torque T and to the mountain torque T_M. We see that the AAM budget in Eq. 5 is very well closed, with the tendency of M (thick solid) coinciding almost exactly with the total torque T (plus). Note also that the total torque is in large part due to the mountain torque T_M (thin solid). In particular, T presents daily oscillations which amplitude is around 10H, and which are essentially due to T_M. Note also that the two tendencies in M_O and M_R (thick grey solid and thick grey dashed) present daily fluctuations that are much more substantial and that reach 100H.

These oscillations between the mass and the wind AAM are not specific of the LMDz-GCM. This is illustrated in the Fig. 2 which presents M, M_O and M_R issued from the ECMWF 10-day forecast starting the 1$^{\text{rst}}$ February 2004, and for which the AAM data have been provided every hour. It shows that the daily oscillations between M_R and M_O are also substantial in the ECMWF model. They compare rather well in amplitude and phase with the corresponding oscillations in the LMDz-GCM (Fig. 1). It is also noticeable that the oscillations of the mass AAM we analyze are also present in the ECMWF analysis (solid line with dots in Fig. 2). This witnesses that they are not related to an initial adjustment of this model at the beginning of the forecasts, and that they are somehow present in the datasets that are used to produce the analysis.

3 Tidal signals responsible for the mass and wind AAM variations

3.1 Methodology and application to M_O

To extract the diurnal and the sub-diurnal signals from the LMDz-GCM we follow a conventional procedure and first build a mean daily cycle for each quantity. For the mean daily cycle of the mass AAM for instance, we evaluate for each 30min in the day, the yearly average of the value of M_O at the same time. From the resulting 48 points half-hourly time series we then subtract the linear trend to ensure a perfect 24h period. We then extract the diurnal and sub-diurnal signals by applying a Fourier decomposition to this mean daily cycle.

The mean daily cycle for M_O (not shown) has an amplitude of 5-6Hd. From minimum to maximum it corresponds to the 10Hd mass AAM daily fluctuations that are directly apparent in Fig. 1a. The semi-diurnal and the diurnal cycles for the mass AAM are shown by the thick dashed line in the Figs. 3a and 3b respectively. Their amplitudes are comparable (around 2-3Hd for both), but their phases differ: the semi-diurnal mass AAM maximum is at $t = 4.5$hr and the diurnal mass AAM maximum is at $t = 7$hr. It is noticeable that the contribution of the shorter periodicities is quite small (not shown): the diurnal and the semi-diurnal signals of M_O explain almost entirely the daily cycle of M_O.

To sample the mean daily cycle from the ECMWF model, we have also used 12 ECMWF 10-day forecasts starting the first day of each month during the year 2004. We have then followed the same procedure to build a mean daily cycle and to extract the diurnal and sub-diurnal signals. The results (not shown) are in good agreement with the diurnal and sub-diurnal cycles from the LMDz-GCM in Fig. 3.

3.2 Semi-diurnal zonal mean diagnostics

According to Eq. 6, M_O strongly depends on the latitudinal distribution of the zonal mean mass $\mathcal{M}$. Its semi-diurnal component is shown in Fig. 4a at four different times separated by a quarter of period. At $t = 4.5$hr, the pattern of $\mathcal{M}$ presents an excess of mass everywhere in the tropical band (i.e. between 30^oS and 30^oN) equilibrated by a deficit of mass everywhere in the midlatitudes and in the polar regions. It is also at this time that the semi-diurnal component of M_O is maximum (Fig. 3a), and this is due to the fact that the atmospheric masses have been moved away from the Earth rotation axis. At all times, the patterns for $\mathcal{M}$ are also rather smooth, and resemble to the geopotential height of the axisymmetric ($s = 0$) Eigensolution of the Laplace tidal's equations with $n = 2$ nodes between the poles (see LH68, Fig. 7). Furthermore, the location of the nodes at $\phi \approx \pm 30^o$ in Fig. 4a indicate that the Lamb parameter $\gamma = \frac{4\Omega^2 r^2}{gH_0}$, of the $n = 2$ Eigensolution in LH68 that fits the best the patterns of of $\mathcal{M}$ is near $\gamma \approx 10$. Here, H_0 is an equivalent depth associated with the vertical structure of the tidal signal associated with $\mathcal{M}$ (see Chapman and Lindzen 1970 and Section 4 below).

The semi-diurnal signal for $\mathcal{U}$ is shown in Fig. 4b. It is everywhere negative at $t = 4.5$hr, thus yielding a negative M_R (not shown). This pattern for $\mathcal{U}$ is also smooth, with minima at $t = 4.5$hr located around $\phi = \pm 50^o$. This again resembles to the zonal wind signal associated with the $n = 2$, $\gamma \approx 10$ Eigensolution shown in LH68 (Fig. 7). The semi-diurnal signal for $\mathcal{V}$ is shown in Fig. 4c, it is antisymmetric with respect to the Equator and with only 1 node between the poles. It also resembles to the meridional wind pattern associated with the $n = 2$, $\gamma \approx 10$ Eigensolution in LH68 (Fig. 7).

It is noticeable that $\mathcal{V}$ is in temporal quadrature with both $\mathcal{M}$ and $\mathcal{U}$. For $\mathcal{M}$ this follows that $\mathcal{V}$ moves the mass in the latitudinal direction according to the mass conservation in Eq. 2: in quadrature before $\mathcal{M}$ is maximum in the Equatorial region, $\mathcal{V}$ is large and positive in the Southern Hemisphere and large and negative in the Northern Hemisphere (at $t = 1.5$hr in Fig. 4c) producing a convergence of masses towards the equatorial band. If we return to the budget for M_O in Fig. 3a, we also see that this pattern for $\mathcal{V}$ produces a maximum of the Coriolis conversion term C at $t = 1.5$hr (dots in Fig. 3a). Notably, the Coriolis conversion is one order of magnitude larger than the torques (thin solid for T_M and plus for T), which explains why the variations in M_O (thick grey) are one order of magnitude larger than those for M (thick black).

Note also that the displacement toward the Equator associated with $\mathcal{V}$ at $t = 1.5$hr in Fig. 4c produces negative tendencies for $\mathcal{U}$ via the Coriolis torque implying that $\mathcal{U} < 0$ almost everywhere a quarter of cycle later (at $t = 4.5$hr in Fig. 4b). Nevertheless, this last argument is only valid if the Coriolis torque dominates the other forcings of the barotropic zonal wind tendency $\partial_t \mathcal{U}$ in Eq. 1. This is confirmed in the Fig. 5 which shows that at $t = 1.5$hr, the Coriolis term (thick grey) almost opposes to the $\mathcal{U}$-tendency (thick black): both are much larger than the sum of the three forcings $\mathcal{F} + \mathcal{T} + \mathcal{B}$ (dots in Fig. 5a), their sum (thin line in Fig. 5a) equals $\mathcal{F} + \mathcal{T} + \mathcal{B}$ almost exactly.

In the context of this budget, the Fig. 5b compares the three forcing terms, $\mathcal{F}$, $\mathcal{T}$, and $\mathcal{B}$ at $t = 2.5$hr. At this time, the semi diurnal mountain torque T_M (thin line in Fig. 3a) is at a maximum and the mountain stress $\mathcal{T}$ is positive everywhere, with a pronounced maximum in the Northern Hemisphere at $\phi \approx 35^oN$ (thick solid). At this time the boundary layer stress $\mathcal{B}$ is substantially smaller than $\mathcal{T}$ (thick dashed), and never becomes substantially larger than at other times (not shown). Although it does not produce a global torque, the momentum flux divergence is also shown in Fig. 5b. Clearly, it induces a redistribution of the angular momentum in latitude, which is locally comparable in amplitude with the effect of the mountain stress $\mathcal{T}$.

3.3 Diurnal zonal mean diagnostics

The diurnal components for $\mathcal{M}, \mathcal{U}$, and $\mathcal{V}$ are more complex than the semi-diurnal components. To clarify their description, we will next split each of them in two parts that are respectively symmetric and antisymmetric with respect to the equator.

The antisymmetric part of $\mathcal{M}$ is shown in Fig. 6a. The first time shown ($t = 5$hr, thick solid line) is also the time at which $\mathcal{M}$ reaches its maximum value in the Northern Hemisphere. This pattern is clearly dominated by a planetary scale structure in which the entire mass in one hemisphere opposes to that in the other. Its structure resembles the height pattern associated with the $n = 1$, $s = 0$ Eigensolution of the Laplace's tidal equations (Fig. 7 in LH68). Note that the anomalies in mass in Fig. 6a are not very pronounced in the polar regions, and have maxima around $\pm 20^o$ suggesting a value for the Lamb parameter around $\gamma \approx 100$ (see again Fig. 7 in LH68). The antisymmetric patterns of $\mathcal{U}$ in Fig. 6b grossly corroborate those for $\mathcal{M}$: they resemble to the zonal wind structure of the $n = 1$ Eigensolution in LH68. As the Eigensolutions that are antisymmetric in geopotential height and zonal wind are symmetric in meridional wind, Fig. 6c shows the diurnal signal of the symmetric part of $\mathcal{V}$. At a given time, the sign of $\mathcal{V}$ is almost independent of latitude and $\mathcal{V}$ has one well defined maximum at the Equator. It thus exchanges mass from one hemisphere to the other. Note also that it is for $\mathcal{V}$ that the resemblance with the $n = 1$, $\gamma \approx 100$ Eigensolution in LH98 is the best.

It is noticeable that this antisymmetric part of the diurnal signal of $\mathcal{M}$ moves the masses from one hemisphere to the other. It does not produce M_0 anomalies because it does not move the masses away from the Earth rotation axis. Similarly, the equatorial antisymmetric part of $\mathcal{U}$ in Fig. 6b does not affect the wind AAM. In agreement with these results, the symmetric patterns for $\mathcal{V}$ in Fig. 6c results in a Coriolis conversion term (C in Eq. 8) that is exactly null.

The symmetric part of the diurnal signal of $\mathcal{M}$ is shown in Fig. 7a. The thick solid line at $t = 7$hr is also the time at which $\mathcal{M}$ is the largest in the Equatorial band. By its shape, this pattern resembles to the geopotential signal associated with the $n = 2$ Eigensolution of the tidal equations. By comparison with LH68, the latitudinal structure of $\mathcal{M}$ in Fig. 7a, suggests a value for the Lamb parameter again near $\gamma \approx 100$. For $\mathcal{U}$ in Fig. 7b, the resemblance with the zonal wind of the $n = 2$ Eigensolution is quite difficult to establish because $\mathcal{U}$ is quite irregular. Nevertheless, note that $\mathcal{U}$ is negative at all latitudes when $\mathcal{M}$ is positive in the Equatorial band, a property it has in common with the zonal wind of the $n = 2$ Eigensolution in LH68. Finally the antisymmetric pattern for the diurnal signal of $\mathcal{V}$ is shown in Fig. 7c. Its shape is rather smooth, and the resemblance with the meridional wind associated with the $n = 2$ Eigensolution is rather good.

The fact that the patterns for $\mathcal{V}$ in Fig. 7c are rather smooth while those for $\mathcal{U}$ in Fig. 7b are much more irregular implies that in the evolution for $\mathcal{U}$ in Eq. 1, the role of the Coriolis force is not as prominent as it is in the semi-diurnal case. This point is illustrated in the Fig. 8a which shows that at $t = 1$hr the forcing term on the lhs of Eq. 1 (thin solid) can become larger than the Coriolis term (thick grey). At this time, this forcing is particularly pronounced around the latitude $\phi = 30^o$N where it is in good part equilibrated by the tendency for the zonal mean barotropic zonal wind $\mathcal{U}$ (thick solid) rather than by the Coriolis term (thick grey).

To establish more precisely which among the three forcings ($\mathcal{F}$, $\mathcal{T}$, or $\mathcal{B}$) is producing the irregular patterns in $\mathcal{U}$, the Fig. 8b compares $\mathcal{F}$, $\mathcal{T}$, and $\mathcal{B}$ at $t = 13hr$. At this time, the diurnal mountain torque is at a maximum (thin line in Fig. 3b), and the mountain stress $\mathcal{T}$ presents a broad maximum in the southern hemisphere subtropics (thick line in Fig. 8b). At the same time, the divergence of the momentum flux $\mathcal{F}$ (thin line in Fig. 8b) presents a pronounced minimum in the NH midlatitudes which amplitude is twice that of the maximum value of $\mathcal{T}$.

$\mathcal{F}$ is also much more irregular than $\mathcal{T}$, and this stays valid at other times (including at $t = 1hr$ as in Fig. 8a, not shown). Accordingly, it is likely that the irregular structures of the $\mathcal{U}$-field in Fig. 7b are in good part related to the forcing by the angular momentum flux divergence.

The AAM budgets associated with the diurnal patterns in Fig. 7 are shown in Fig. 3b. In it, we see that the $\mathcal{V}$ pattern at $t = 1hr$ is almost at a maximum of the Coriolis conversion terms C (dots in Fig. 3b). Here again, note that the Coriolis conversion term C is one order of magnitude larger than the total torque T.

4 Interpretation with a shallow water model

4.1 Model description and experimental set-up

The fact that the barotropic zonal mean flow responsible for the large daily fluctuations in M_R and M_O resembles to the Eigensolutions of the shallow water equations suggests that the stresses in the LHS of Eq. 1, are associated with zonal mean zonal forces which trigger these resonant modes of motion. To illustrate how this can occur, we consider a very simplified model, where a zonally symmetric atmosphere responds to a small zonal mean dynamical forcing $\overline{X}$. If we assume an atmosphere that is isothermal at rest, the response to $\overline{X}$ can be described using the hydrostatic linear set of equations:

$$\rho_0 \frac{\partial \overline{u}}{\partial t} - 2\Omega \sin \phi \, \rho_0 \overline{v} = \overline{X}, \tag{9}$$

$$\rho_0 \frac{\partial \overline{v}}{\partial t} + 2\Omega \sin \phi \, \rho_0 \overline{u} = -\frac{g}{r} \frac{\partial \overline{h}}{\partial \phi} \tag{10}$$

$$\frac{\partial}{\partial t} \left(\frac{\partial \overline{h}}{\partial z} + (1 - \kappa) \frac{\overline{h}}{H} \right) + \frac{\kappa}{H} \rho_0 \overline{w} = 0 \tag{11}$$

$$\frac{\partial}{\partial t} \frac{\partial \overline{h}}{\partial z} - \frac{1}{r \cos \phi} \frac{\partial}{\partial \phi} \cos \phi \rho_0 \overline{v} - \frac{\partial}{\partial z} \rho_0 \overline{w} = 0 \tag{12}$$

In Eqs. 9–12, $\overline{u}$, $\overline{v}$, and $\overline{w}$ are the three components of the zonal mean wind, $\rho_0 = \exp(-z/H)$ is a non-dimensional profile for the basic density, and H is the mean scale height $H = RT_r/g$ (where T_r is the temperature of the atmosphere at rest and R is the gas constant for dry air). Finally, $\kappa = R/c_p = 2/7$ where c_p is the specific heat at constant pressure, and the zonal mean pressure has been written $\overline{p} = \rho_r g \overline{h}$, where $\rho_r = 1\mathrm{kg}\ \mathrm{m}^{-3}$ is a constant reference density.

If we now assume that the forcing function is separable in the vertical direction and can be written

$$\overline{X} = \tilde{X}(t, \phi) \exp(-z/2H - \beta z), \tag{13}$$

where $\tilde{X}$ is a real function, a particular solution to the set of Eqs. 9–12 can be searched in the form:

$$\left(\rho_0 \overline{u}, \rho_0 \overline{v}, \rho_0 \overline{w}, \overline{h} \right) = \left(\tilde{u}, \tilde{v}, \tilde{w}, \tilde{h} \right) (t, \phi) \exp(-z/2H - \beta z). \tag{14}$$

After substitution, this yields to the linearized shallow water system,

$$\frac{\partial \tilde{u}}{\partial t} - 2\Omega \sin \phi \, \tilde{v} = \tilde{X}, \tag{15}$$

$$\frac{\partial \tilde{v}}{\partial t} + 2\Omega \sin \phi \, \tilde{u} = -\frac{g}{r} \frac{\partial \tilde{h}}{\partial \phi}, \tag{16}$$

$$\frac{\partial \tilde{h}}{\partial t} + \frac{H_0}{r \cos \phi} \frac{\partial}{\partial \phi} \cos \phi \, \tilde{v} = 0, \tag{17}$$

where H_0 is the equivalent depth:

$$H_0 = \frac{\kappa H}{1/4 - \beta^2 H^2}. \tag{18}$$

When $\tilde{X} = 0$, the Eqs. 15–17 are the equations for the tides with zonal wavenumber zero (LH68).

To analyze the response to the forcing $\tilde{X}$ we solve the shallow-water set of Eqs. 15–16 with the finite difference model described in Lott and d'Andrea (2005). To specify $\tilde{X}$ we take from the GCM the semi-diurnal and the diurnal cycles of the stresses $\mathcal{F}$, $\mathcal{T}$, and $\mathcal{B}$ in Eq. 4 (see also Figs. 5b and 8b) and equal each of them to the stress due to $\overline{X}$ in Eq. 9. More specifically, and to mimic the mountain forcing for instance, we evaluate the surface stress associated with the zonal force $\overline{X}$ and equal it to $\mathcal{T}$:

$$\int_0^\infty \rho_r \overline{X} dz = \frac{\rho_r \tilde{X}}{\frac{1}{2H} + \beta} = \mathcal{T}. \tag{19}$$

Using Eq. 13, this yields to $\tilde{X} = \frac{\mathcal{T}}{\rho_r H_0}$ in the barotropic case in Section 4.2, and $\tilde{X} = \frac{2\kappa \mathcal{T}}{\rho_r H_0}$ in the baroclinic case in Section 4.3. Then, the shallow water model is integrated over one year, with the amplitude of the forcing increasing smoothly and uniformly during the first six months. This reduces the influence of the spin-up in the model, and ensures that the period of the response at the end of the simulation is exactly that of the forcing. We then analyze the response to each forcings ($\mathcal{F}$, $\mathcal{T}$, and $\mathcal{B}$) looking at the last day of the simulations.

4.2   Barotropic configuration and semi-diurnal response

If we take for the parameter β the value $\beta = \frac{1-\kappa}{H} - \frac{1}{2H}$, then, the equivalent depth $H_0 = \frac{H}{1-\kappa}$ and the thermodynamic Eq. 11 implies that our particular solution $\overline{w} = 0$: this solution satisfies as well a free slip lower boundary condition, and has the vertical structure of a Lamb wave (Lamb 1932). In this configuration the Eqs. 15–17 satisfy the AAM budget:

$$\frac{d}{dt}(M_R + M_O) = T_X, \tag{20}$$

where the wind AAM, the mass AAM, and the torque due to X are:

$$M_R = 2\pi r^3 \int_{-\pi/2}^{+\pi/2} \cos^2\phi \, \rho_r H_0 \tilde{u} \, d\phi, \quad M_O = 2\pi r^4 \Omega \int_{-\pi/2}^{+\pi/2} \cos^3\phi \, \rho_r \tilde{h} \, d\phi, \text{ and} \tag{21}$$

$$T_X = 2\pi r^3 \int_{-\pi/2}^{+\pi/2} \cos^2\phi \, \rho_r H_0 \tilde{X} \, d\phi. \tag{22}$$

This AAM budget is very close to the AAM budget in Eqs. 5, replacing (i) $\mathcal{U}$ in the definition of M_R in Eq. 6 by $\rho_r H_0 \tilde{u}$, (ii) $\mathcal{M}$ in the definition of M_O by $\rho_r \tilde{h}$, and (iii) the stresses ($\mathcal{F}$, $\mathcal{T}$ or $\mathcal{B}$) in the definition of the torques in Eq. 7 by $\rho_r H_0 \tilde{X}$. Similarly, a separate budget for the mass AAM can be written,

$$\frac{dM_O}{dt} = C, \text{ where } C = -4\pi r^3 \Omega \int_{-\pi/2}^{\pi/2} \cos^2\phi \, \sin\phi \, \rho_r H_0 \tilde{v} \, d\phi. \tag{23}$$

Here the Coriolis conversion term is as in Eq. 8 replacing $\mathcal{V}$ by $\rho_r H_0 \tilde{v}$.

The semi-diurnal evolution of the AAM budget in the shallow water model is presented in Fig. 9 when $H_0 = 9.5$km. When the forcing $\tilde{X}$ is keyed to the mountain stress $\mathcal{T}$, the mass AAM tendency (dM_O/dt thick grey solid) presents a semi-diurnal cycle that far exceeds the corresponding cycle in the absolute AAM tendency (dM/dt thick solid). This comparatively large daily cycle is due to the fact that the Coriolis conversion term (C, black dots) far exceeds the mountain torque (T_X, plus). The corresponding amplitude of the cycle in M_O is around 2Hd (thick grey in Fig. 9b), a value quantitatively comparable with the semi diurnal signals seen in the mass AAM from the LMDz-GCM (Fig. 3a). Note also that the phase is almost correct with a maximum in M_0 at t=5.5h (Fig. 9a), while the maximum for M_O in the LMDz-GCM is at t=4.5h (Fig. 3a).

8

To establish the significance of the other forcings, the Fig. 9b shows the mass AAM cycles when $\tilde{X}$ is keyed to $\mathcal{F}$ and $\mathcal{B}$. The amplitude of the M_O-response to $\mathcal{F}$ is also quite large (grey dashed in Fig. 9b) but the phase is almost in phase opposition with that found in the LMDz-GCM (Fig. 3a). Finally, note that the response when the shallow water model is keyed to $\mathcal{B}$ is significantly smaller than the two others (grey dots in Fig. 9b). This naturally follows that the boundary layer stress is by far the smallest stress at the semi-diurnal period (Fig. 5b).

The fields $\rho_r g \tilde{h}$, $\rho_r H_0 \tilde{u}$, and $\rho_r H_0 \tilde{v}$ associated with the semi-diurnal mountain stress $\mathcal{T}$ are shown in the Fig. 10. As for the semi-diurnal zonal mean and barotropic fields from the LMDz-GCM in Fig. 4, the shallow water model response resembles to the second gravest mode ($n = 2$) Eigensolution of the axisymmetric ($s = 0$) Laplace's tidal equations shown in the Fig. 7 of LH68. The best correspondence is with the $n = 2$ Eigensolution associated with a Lamb parameter $\gamma = 10$, which follows that the value $H_0 = 9.5$km yields to $\gamma \approx 9.3$. Note also that the amplitudes of all the fields from the shallow water model match relatively well the corresponding fields from the GCM in Fig. 4.

4.3 Sensitivity test to the value of H_0

To understand the shallow water model response, it is mandatory to refer to the Fig. 1 from LH98, where the dispersion curves for the $s = 0$ Eigensolutions of the Laplace's tidal equations are shown. From this figure, we can deduce that for the semi-diurnal frequency, $\sigma/2\Omega = 1$, the Eigenvalues of the Lamb parameters γ_n increases with n and the values of the leading ones are given by:
$$\gamma_1 \approx 3 < \gamma_2 \approx 10 < \gamma_3 \approx 25 < \cdot\cdot < \gamma_n < \gamma_{n+1} < \cdots. \tag{24}$$

When $H_0 = 9.5$km, the Lamb parameter $\gamma = 9.3$, which means that the semi-diurnal forcing is in near resonance with the $n = 2$ Eigenmode. Note also that the forcing is subcritical regarding this Eigensolution, in the sense that the semi-diurnal frequency is smaller than the period of the $n = 2$ Eigensolution of the shallow water equation.

Because of this resonant behavior, it is important to analyze the sensitivity of our result to the choice of H_0. This is done in the Fig. 11 which shows the maximum amplitude and the phase of the mass AAM response when the forcing $\tilde{X}$ is keyed to the semi-diurnal mountain stress $\mathcal{T}$. We see that there is a large range of values for H_0 (from 9.2km to 10km) that leads to maxima in M_0 around $M_O \approx 1-3$Hd: our choice for H_0 is not the one for which the resonant amplification is extremely large (i.e; around $H_0 \approx 8.9$km). Note also that the phase (i.e., the time at which M_O reaches its maximum value) is almost insensitive to the value of H_0, and as long as our forcing is subcritical. Nevertheless, note that the whole response changes sign (e.g. the time of the maximum for M_O shifts by 6hr) when the forcing becomes supercritical (here when $H_0 < 8.9$km).

4.4 Baroclinic configuration and diurnal response

If in the same configuration we impose diurnal forcings in the shallow water model (not shown), the response resembles to an $n = 1$ Eigensolution of the tidal Equations but its amplitude is very small compared to the corresponding signal from the GCM in Fig. 6. To understand this more precisely, it is mandatory to recall that for the diurnal frequency $\sigma/2\Omega = 0.5$ the leading Eigenvalues of the Lamb parameters are (from Fig. 1 in LH68):

$$\gamma_1 \approx 25 < \gamma_2 \approx 150 < \gamma_3 \approx 400 < \cdot\cdot < \gamma_n < \gamma_{n+1} < \cdots. \tag{25}$$

Hence the response of the shallow water model follows that when $\gamma = 9.8$ the closest eigenvalue of the Lamb parameter is indeed for the gravest mode $\gamma_1 = 25$ but is quite far from it.

To produce more substantial diurnal signals, one needs to consider diurnal forcings imposing a more baroclinic response. In the simplified model (Eqs. 15-17), this can be done by taking for β a pure imaginary value $\beta = i\beta'$ where β' is real. In this case the forcing changes sign at the altitude π/β', it decays more rapidly with altitude than in the barotropic case, and $H_0 = \frac{\kappa H}{1/4 + \beta'^2 H^2}$ can be substantially smaller than before. Although it maintains an attracting simplicity, our shallow water model has in this case an important defect: $\tilde{w}$ is not null at the ground so the solution in Eq. 14 can only be a part of the forced solution. As we are in a linear framework, we must add to it a solution that is not forced inside the flow, but which vertical velocity at the ground opposes to $\tilde{w}$. If we neglect it, nearly half $(1 - 2\kappa = 3/7$ more exactly) of the meridional mass flux associated with the solution in Eq. 14 passes through the lower boundary instead of changing the atmospheric mass $\rho_r \tilde{h}$. This omission has a direct effect on the AAM budget which now write:

$$\frac{d}{dt}\left(M_R + \frac{1}{2\kappa}M_O\right) = T_X , \tag{26}$$

where the wind AAM and the torque due to X are:

$$M_R = 2\pi r^3 \int_{-\pi/2}^{+\pi/2} \cos^2\phi \rho_r \frac{H_0}{2\kappa}\tilde{u}d\phi , \quad T_X = 2\pi r^3 \int_{-\pi/2}^{+\pi/2} \cos^2\phi \rho_r \frac{H_0}{2\kappa}\tilde{X}d\phi . \tag{27}$$

while the mass AAM is as in Eq. 21. Its separate budget is given by:

$$\frac{d}{dt}\frac{M_O}{2\kappa} = C , \quad \text{with} \quad C = -4\pi r^3 \Omega \int_{-\pi/2}^{\pi/2} \cos^2\phi \sin\phi \, \rho_r \frac{H_0}{2\kappa}\tilde{v}d\phi . \tag{28}$$

Again, this AAM budget is very close to the actual AAM budget in Eqs. 5, (i) taking for $\mathcal{U}$ in the definition of M_R in Eq. 6 the value $\rho_r \frac{H_0}{2\kappa}\tilde{u}$, (ii) taking for $\mathcal{M}$ in the definition of M_O the value $\rho_r \tilde{h}$, (iii) taking for the stresses ($\mathcal{F}$, $\mathcal{T}$, and $\mathcal{B}$) in the definition of the torques in Eq. 7) the value $\rho_r \frac{H_0}{2\kappa}\tilde{X}$, and (iv) taking for $\mathcal{V}$ in the definition of the Coriolis conversion term in Eq. 8 the value $\rho_r \frac{H_0}{2\kappa}\tilde{v}$.

4.4.1 $H_0 = 2.5$km, $n = 1$ response to $\mathcal{T}$

If the first zero of the diurnal forcing in Eq. 13 is near $\pi/\beta' \approx 30$km, the altitude $H_0 = 2.5$km, the Lamb parameter $\gamma \approx 35$ is closer to the diurnal value for $\gamma_1 \approx 25$, and the diurnal forcing is supercritical with regard to the $n = 1$ Eigensolution. In this case, the response of the shallow water model when $\tilde{X}$ is keyed to each of the three stresses $\mathcal{T}$, $\mathcal{F}$, and $\mathcal{B}$ is dominated by a $n = 1$ Eigensolution of the $s = 0$ Laplace's tidal equations. Again, the largest responses are those associated with the mountain stress $\mathcal{T}$ and the angular momentum flux divergence $\mathcal{F}$. It is also for $\mathcal{T}$ that the phase agreement To illustrate this point, the Figs. 12a–b show the equatorially-antisymmetric patterns for the surface pressure $\rho_r g\tilde{h}$ and for the zonal momentum $\rho_r \frac{H_0}{2\kappa}\tilde{u}$ when $\tilde{X}$ is keyed to $\mathcal{T}$. Fig. 12c show the equatorially-symmetric patterns of the meridional mass flux $\rho_r \frac{H_0}{2\kappa}\tilde{v}$.

Clearly, for $\rho_r \frac{H_0}{2\kappa}\tilde{v}$ in Fig. 12c the agreement with $\mathcal{V}$ from the LMDz-GCM in Fig. 6c is quite good both in phase and amplitude. For the zonal wind in Fig. 12b, the resemblance is not as pronounced but stays fairly good, in particular, the location of the jet maxima around $\pm 30^o$ is rather well reproduced. Finally, the surface pressure pattern from the shallow water model in Fig. 12a also has a good shape, but the amplitude is almost half that of the corresponding quantity in Fig. 6a. This mismatch with the mass fields from the GCM, while the velocity fields compare in amplitude is again associated with the fact that the forced solution in the shallow water model only translates 2κ of the meridional mass flux $\rho_r \frac{H_0}{2\kappa}\tilde{v}$ into mass $\rho_r \tilde{h}$.

As for the barotropic case, we have also checked that the value for H_0 chosen is not strictly ad-hoc, in the sense that it is not the value for which an extremely strong response occurs. Finally, as the shallow water model response is largely dominated by the antisymmetric responses in mass and zonal wind shown in Figs. 12a–b, it does not present signals in mass and wind AAM tendencies exceeding substantially the diurnal cycle of the total torque T.

4.4.2 $H_0 = 1$km, $n = 2$ response to $\mathcal{F}$

To produce a diurnal response with amplified signals in mass and wind AAM, we have to consider that a fraction of the diurnal forcing is even more baroclinic than in the previous section. In the shallow water model, this can be done by considering that the first zero of the forcing is near $\pi/\beta' \approx 17$km. In this case, $H_0 = 1$km, $\gamma \approx 90$ is relatively close to $\gamma_2 \approx 150$, and the diurnal forcing is subcritical with regard to the $n = 2$ Eigensolution.

In this case, the strongest signal are still obtained when $\tilde{X}$ is keyed to $\mathcal{T}$ and $\mathcal{F}$. To document in one case the structure of the response when the forcing follows the angular momentum flux divergence, the Figs. 13a–b show the equatorially-symmetric patterns for the surface pressure $\rho_r g \tilde{h}$ and for the zonal momentum $\rho_r \frac{H_0}{2\kappa} \tilde{u}$ resulting from the diurnal cycle in $\mathcal{F}$ when $\tilde{X}$ is keyed to $\mathcal{F}$. The Fig. 13c show the equatorially-antisymmetric patterns of the meridional mass flux $\rho_r \frac{H_0}{2\kappa} \tilde{v}$ in the same configuration.

Again, it is for the meridional mass flux from the shallow water model ($\rho_r \frac{H_0}{2\kappa} \tilde{v}$ in Fig. 13c) that the resemblance with the GCM is the best ($\mathcal{V}$ in Fig. 7c). More specifically, in both models, the two extrema for this quantity are located around $\pm 30^o$. The comparison between the barotropic zonal winds in the ($\rho_r \frac{H_0}{2\kappa} \tilde{u}$ in Figs.7b and $\mathcal{U}$ in 13b) is quite difficult, because these fields are rather erratic in both models. This propensity for the momentum flux divergence to produce irregular zonal wind fields was found to be quite systematic (e.g. it does occur for all values of H_0). If we put this in relation with the fact that in the diurnal zonal mean budget, the signal for $\mathcal{F}$ exceeds in some places the Coriolis force $2\Omega \sin \phi \mathcal{V}$ and is much more irregular (see the Eq. 1, the Fig. 8b and the corresponding discussion in Section 3.3), this suggests that the irregularities in the zonal wind from the LMDz-GCM in Figs.7b are related to the angular momentum forcing. Finally, the patterns for the surface pressure from the shallow water model in Fig.13 also compare relatively well with with those from the GCM (once taken into account the 2κ factor on the amplitude discussed above). In particular, the nodes at $\pm 30^o$ are well located. Nevertheless, in the shallow water model the signal in the polar latitudes is very small, while it is significant in the LMDz-GCM. This difference is strongly suggestive that we have decreased too much H_0 to obtain a diurnal signal with a realistic amplitude.

It is also of interest to notice that in this baroclinic case the shallow water solution forced by $\mathcal{F}$ can produce mass AAM variations that compare with those from the GCM. This point is illustrated in Fig. 14 which shows the mass AAM cycle associated with the response displayed in Fig. 13. We see that the mass AAM reach 1Hd, and is entirely driven by a Coriolis conversion term (C dots) which value is around $10 - 15$H, again one order of magnitude larger than the daily cycle of the torque (Fig. 3b).

5 Conclusion
5.1 Summary
A 1-year integration done with the LMDz-GCM has been used to analyze the axial angular momentum budget at the diurnal and sub-diurnal periodicities. The model results have been compared with 12 ECMWF 10-days forecasts and some ECMWF analysis products.

As the surface pressure tides result in longitudinal pressure gradients across the major mountain ranges, they give rise to a surface stress $\mathcal{T}$ acting on the zonal mean barotropic flow (Eqs. 1 and 4). Globally, this mountain stress results in a mountain torque T_M that has a daily cycle of few Hadleys (Eq. 7 and Fig. 1b). This translates in a daily cycle for the total torque T of the same magnitude, the daily cycle of the the boundary layer torque T_B being substantially smaller than that of T_M. The daily cycle of T produces variations in the total angular momentum (M) that are almost one order of magnitude below 1Hd, e.g. that are very small compared to the amplitude of the natural variations of M. Nevertheless, this very small daily signal in M results in fact from the cancellation between much stronger daily cycles of the mass AAM M_O and of the wind AAM M_R (their amplitudes are of few Hds, see Fig. 1 for the LMDz-GCM, and Fig. 2 for the ECMWF forecasts and analysis).

To interpret these large and almost canceling oscillations, we have diagnosed from the LMDz-GCM, the diurnal and semi-diurnal cycles of three zonal mean and barotropic fields, $\mathcal{M}, \mathcal{U}$, and $\mathcal{V}$, which latitudinal distributions are directly related to the mass AAM (M_O), to the wind AAM (M_R), and to the conversion between them (C) respectively.

The semi-diurnal signals in $\mathcal{M}, \mathcal{U}$, and $\mathcal{V}$ are almost like the $n = 2$ zonally symmetric ($s = 0$) Eigensolution of the Laplace's tidal equations. It corresponds to a redistribution of masses ($\mathcal{M}$) from the midlatitudes and polar regions toward the Equatorial band (Fig. 4a) that results in variations of the mass AAM M_O of a few Hds (Fig. 3a). It also corresponds to variations in the zonal wind $\mathcal{U}$ with two extrema in the mid-latitudes of the same sign (Fig. 4b), which results in large variations of the wind AAM M_R. Via the conservation of the zonal mean of the atmospheric mass, $\mathcal{M}$ is driven by the transport of meridional mass $\mathcal{V}$ (shown in Fig. 4c), while $\mathcal{U}$ is also driven by $\mathcal{V}$ via the Coriolis torque (because the latter dominates the other forcing terms of the $\mathcal{U}$ tendency in the zonal mean of the zonal momentum budget see Fig. 5). In terms of the AAM budget, this driving role of $\mathcal{V}$ via the conservation of the mass and via the Coriolis force implies that the Coriolis conversion term C is one order of magnitude larger than the torque T in the separate semi-diurnal budgets of M_O and M_R (Fig. 3a).

The diurnal signals in $\mathcal{M}, \mathcal{U}$, and $\mathcal{V}$ are more complex to interpret, so we separate for each fields its symmetric part and its anti-symmetric part with respect to the Equator.

The Equatorially antisymmetric diurnal cycles of $\mathcal{M}$ and $\mathcal{U}$, as well as the Equatorially symmetric diurnal cycle of $\mathcal{V}$, are quite substantial and reminiscent of an $n = 1$ $s = 0$ Eigensolution of the Laplace's tidal equation. By construction, they cannot be associated with variations in axial mass AAM or wind AAM, and the symmetric part of $\mathcal{V}$ produces no Coriolis conversion between them.

For $\mathcal{M}$, the Equatorially symmetric patterns in Fig. 7a also resemble to the $n = 2$ zonally symmetric ($s = 0$) Eigensolution of the Laplace's tidal equations. The same is true for the antisymmetric part of $\mathcal{V}$ in Fig. 7c. Nevertheless, the Equatorially symmetric part of $\mathcal{U}$ in Fig. 6b is quite irregular in latitude when compared for instance with the symmetric part of $\mathcal{V}$ in Fig. 6c. This follows from the fact that the angular momentum flux divergence in the right hand side of the zonal momentum Eq. 1 is as large as the Coriolis term $2\Omega \sin \phi \mathcal{V}$. Nevertheless, and for the same reason than for the semi-diurnal signals, these different patterns explain the large but opposite daily cycles in mass and wind AAM (Fig. 3b).

We have then postulated that these large and compensating diurnal and semi-diurnal oscillations in M_O and M_R results from a dynamical excitation of axisymmetric free modes of oscillation, and that this dynamical forcings are also associated with the surface stresses that affect the zonal mean angular momentum budget (Eq. 1). To support this hypothesis, we have used a shallow water model driven by dynamical forcings which vertical integral equal the

various zonal mean zonal stresses extracted from the LMDz-GCM (Eq.19).

If the shallow water model configuration is barotropic (taking for the equivalent depth $H_0 = 9.5$km), a semi-diurnal forcing keyed to the mountain stress induces a response associated with mass and wind AAM oscillations (Fig. 9a) consistent in amplitude and phase with the semi-diurnal oscillations seen in the LMDz-GCM (Fig. 1c). In the shallow water model, the response is also dominated by a planetary mode of oscillation that is very similar to the $n = 2$ and $s = 0$ Eigensolution of the Laplace's tidal equations (Fig. 10), and that is also very near the GCMs results (Fig. 4). These results follow that in the shallow water model, the semi-diurnal frequency is not far from the eigenfrequency of the $n = 2$ Eigensolution. We also find a substantial $n = 2$ response when the shallow water model forcing is keyed to the angular momentum flux divergence $\mathcal{F}$, but we find a substantially smaller response when it is keyed to the boundary layer stress $\mathcal{B}$. These results stay qualitatively unchanged when we vary the shallow water model depth, H_0, between 9.2km and 10km.

To obtain substantial effects at the diurnal frequency in the shallow water model, we need to consider a more baroclinic set-up. For instance, if we take for H_0 a value around $H_0 = 2.5$km, the diurnal response when the shallow water model forcing is keyed to the mountain stress $\mathcal{T}$ is dominated by a zonally symmetric planetary scale pattern which is almost like an $n = 1$ Eigensolution of the $s = 0$ Laplace's tidal equations (Fig. 12). The shallow water model response is also close to the zonal mean and barotropic diurnal signal in the LMDz-GCM, for which the $\mathcal{M}$ and $\mathcal{U}$ patterns are antisymmetric with respect to the Equator, and $\mathcal{V}$ is symmetric with respect to the Equator (Fig. 6). Again the shallow water model response is comparable when the forcing is keyed to $\mathcal{F}$, but substantially smaller when it is keyed to $\mathcal{B}$. By its $n = 1$-structure, this response from the shallow water model does not produce amplified signals in mass and wind AAMs.

To produce amplified diurnal signals in mass and wind AAMs in the shallow water model, one needs to consider an even more baroclinic set up, taking for instance $H_0 = 1$km. In this case the response to all the stresses is dominated by large scale circulation patterns resembling to the $n = 2$ Eigensolution of the Laplace's tidal equations. In this case, a good fit with the results from the LMDz-GCM in Fig. 7 are when the forcing is keyed to the divergence of the momentum flux $\mathcal{F}$ (Figs. 13 and 14). The simulation with the shallow water model nevertheless shows a signal that is rather small at high latitudes compared to the LMDz-GCM diurnal signal in Fig. 7. According to the shapes of the Eigensolutions in the Fig. 7 of LH68, this indicates that we have decreased H_0 too much. Interestingly, the barotropic zonal wind in the shallow water model response to $\mathcal{F}$ (Fig. 13b) also presents a rather irregular structure. This irregular structure is reminiscent of the one found for $\mathcal{U}$ in the GCM (Fig. 7b), and this illustrates that divergence of the momentum flux also plays a significant role in our problem.

5.2 Significance for Geodesy and for the theory of tides

The results we presented have two potential domains of application: geodesy and the theory of the atmospheric tides.

Concerning Geodesy, it is noticeable that nowadays the measurements of the Earth orientation parameters become increasingly precise (Rotacher et al. 2001, Schreiber et al. 2004). Accordingly, the analysis of the different terms that affect their diurnal and sub-diurnal changes is an important topic of research (Rotacher et al. 2001). To estimate the atmospheric contribution, two methods have been used: the momentum approach and the torque approach. In the first, the AAM of the atmosphere is evaluated directly from atmospheric reanalysis and the

Earth+Ocean angular momentum varies to equilibrate the AAM changes. In the second, the torque of the atmosphere on the Earth is evaluated directly from a combination of atmospheric analysis and short-range forecasts. Although the two methods should give exactly the same results, they present large discrepancies at the diurnal and sub-diurnal periodicities (deViron et al. 2005). The presence of the large canceling terms between the mass AAM tendency and the wind AAM tendency documented in this paper are probably at the origin of these errors for the axial component of the AAM budget.

Still in the context of geodesy, it is noticeable that our axisymmetric modes exert an axisymmetric pressure force on the Earth Surface. In particular, the semi-diurnal and the diurnal modes with $n = 2$ can modify the Earth ellipticity at the corresponding periods. For the same reason, the diurnal mode with $n = 1$ can affect the diurnal cycle of the geocenter position along the rotation axis.

Our results also have some implications for the theory of the atmospheric tides. In the observations, the diurnal and semi-diurnal $s = 0$ tidal signal in surface pressure is close to 10Pa (Dai and Wang 1999). Although it represents only 10% of the surface pressure tide, this value is not negligible: it corresponds in amplitude to the gravitational (lunar) tide (Goulter 2005). If we assume that the LMDz-GCM has a rather realistic diurnal tidal signal, and as we reproduce rather well in phase and amplitude the $s = 0$ surface pressure signal with our shallow water model, we have established here that the dynamical forcings of the zonal mean zonal flow can force a good part of the $s = 0$ surface pressure tide.

It is quite clear nevertheless that our reproduction, with a linearized shallow water model of those axi-symmetric and barotropic tidal signals, is not a definite proof that they are due to the forcings analyzed in this paper. To establish this more precisely, one should use a more complete tidal model (see for instance Hagan 1996, Hagan and Forbes 2001) and analyze its axisymmetric response to all the possible zonal mean forcings (e.g., dynamical as well as thermodynamical). The latitudinal and vertical structures of these forcings could also be deduced from the GCM, as it has been done here for the latitudinal structures only.

References

Barnes R. T. H., R. Hide,A. A. White, and C. A. Wilson, 1983: Atmospheric angular momentum fluctuations, length-of-day changes and polar motion, *Proc. R. Soc. London*, **A387**, 31-73.

Chao, B. F., 1989: Length of day variations caused by El Niño/Southern Oscillation and Quasi Biennal Oscillation, *Geophys. Res. Lett.*, **11**, 541–544.

Chapman, S. and R. S. Lindzen, 1970: Atmospheric tides, *D. Reidel Publishing Company*, 200pp.

Dai, A. and J. Wang, 1999: Diurnal and semidiurnal tides in global surface pressure fields, *J. Atmos. Sci.*, **56**, 3874–3891.

deViron, O., G. Schwarzbaum, F. Lott, and V. Dehan, 2005: Diurnal and sub-diurnal effects of the atmosphere on the Earth Rotation and geocenter motion, *J. Geophys. Res.*, **110,** D22107, doi: 10.1029/2005JD006073.

Egger, J., 2003: Gravity wave drag and global angular momentum: geostrophic adjustment processes, *Tellus A*, **55,** 419-425, DOI: 10.1034/j.1600-0870.2003.00024.x

Frei, Ch. and H. C. Davies, 1993: Anomaly in the Alpine diurnal pressure signal: observations and theory, *Quart. J. Roy. Meteor. Soc.*, **119,** 1269–1289.

Goulter, S. W., 2005: The structure of the lunar semi-diurnal pressure tide L2, *Quart. J. Roy. Meteor. Soc.*, **131,** 723-758. doi: 10.1256/qj.03.234.

Hagan, M. E., 1996: Comparative Effects of migrating solar sources on tidal signatures in the middle and upper atmosphere, J. Geophys. Res., 101, 21,213-21,222.

Hagan, M. E., and J. M. Forbes, 2002: Migrating and nonmigrating diurnal tides in the middle and upper atmosphere excited by tropospheric latent heat release, J. Geophys. Res., 107(D24), 4754, doi:10.1029/2001JD001236.

Hendon, H. H., 1995: Length of day changes associated with the Madden–Julian oscillation, J. Atmos. Sci., **52**, 2373–2383.

Hourdin, F., I. Musat, S. Bony, P. Braconnot, F. Codron, J.-L. Dufresne, L. Fairhead, M.-A. Filiberti, P. Friedlingstein, J.-Y. Grandpeix, G. Krinner, P. Levan, and F. Lott, 2006: The LMDZ4 general circulation model: climate performance and sensitivity to parametrized physics with emphasis on tropical convection, *Climate Dynamics*, **27**, 787-813, 10.1007/s00382-006-0158-0.

Iskenderian, H., and D. A. Salstein, 1998: Regional sources of mountain torque variability and high frequency fluctuations in atmospheric angular momentum, *Mon. Wea. Rev.*, **126**, 1681–1694.

Lamb, H., 1932: Hydrodynamics, *Cambridge University Press.*

Lejenäs, H., and R. A. Madden, 2000: Mountain torques caused by normal-mode global Rossby waves, and the impact on atmospheric angular momentum, *J. Atmos. Sci.*, **57**, 1045–1051.

Longuet-Higgins, M. S, 1968: The eigenfunctions of Laplace's tidal equations over a sphere, *Phil. Trans. Roy. Soc. London*, **A262**, 511–607.

Lott, F., A. W. Robertson and M. Ghil, 2001: Mountain torques and atmospheric oscillations, *Geophys. Res. Lett.*, **28**, 1207–1210.

Lott, F., A. W. Robertson, and M. Ghil, 2004a: Mountain torques and Northern-Hemisphere low-frequency variability Part I: Hemispheric aspects, *J. Atmos. Sci.*, **61**, 1259–1271.

Lott, F., A. W. Robertson and M. Ghil, 2004b: Mountain torques and Northern-Hemisphere low-frequency variability Part II: Regional and episodic aspects, *Journal of the Atmospheric Sciences*, **61**, 1272-1283.

Lott, F. and F. d'Andrea, 2005: Mass and wind axial angular momentum responses to mountain torques in the 1–25 day band. Links with the Arctic Oscillation, *Quart. J. Roy. Meteor. Soc.*, **131**, 1483–1500, doi: 10.1256/qg.03.168.

Lott, F.,L. Fairhead, F. Hourdin and P. Levan, 2005a: The stratospheric version of LMDz: Dynamical Climatologies, Arctic Oscillation, and Impact on the Surface Climate. *Climate Dynamics*, **25**, 851–868. DOI: 10.1007/s00382-005-0064-x.

Lott, F., L. Goudard and A. Martin, 2005b: Links between the mountain torque and the Arctic Oscillation in the Laboratoire de Meteorologie Dynamique (LMDz) general circulation model, *Journal of Geophysical Research*, **110**, D22107, doi: 10.1029/2005JD006073. Madden, R. A., 1987: Relationship between changes in the length of day and the 40 to 50-day oscillation in the tropics, *J. Geophys. Res.*, **92**, 8391–8399.

Rothacher, M., G. Beutler, R. Weber, and J. Hefty, 2001: High-frequency variations in Earth rotation from global positionning data, *J. Geophys. Res.*, **106,** 13711–13738, doi:10.1029/2000JB900393.

Schreiber, K.U., A. Velikoseltsev, M. Rothacher, T. Klugel, G. E. Stedman, and D. L. Wiltshire, 2004: Direct measurement of diurnal polar motion by ring laser gyroscopes, *J. Geophys. Res.*, **109,** B06405, doi:10.1029:/2003JB002803.

Tanaka, H. L. and Kasahara, A., 1992: On the normal modes of Laplace's tidal equations for zonal wavenumber zero, *Tellus,* **44a,** 18–32.

Thompson, D. W., and J. M. Wallace, 1998: The Arctic Oscillation signature in the wintertime geopotential height and temperature fields, *Geophys. Res. Lett.*, **25**, 1297-1300.

von Storch, J.-S., 1999: The reddest atmospheric modes and the forcing of the spectra of these modes, *J. Atmos. Sci.*, **56**, 1614–1626.

von Storch, J.-S., 2001: How do friction and pressure torques affect the relative Ω angular momenta of the atmosphere, *J. Atmos. Sci.*, **58**, 1995–1999.

Weickmann, K. M., G. N. Kiladis and P. D. Sardeshmukh, 1997: The dynamics of intraseasonal atmospheric angular momentum oscillations, *J. Atmos. Sci.*, **54**, 1445–1461.
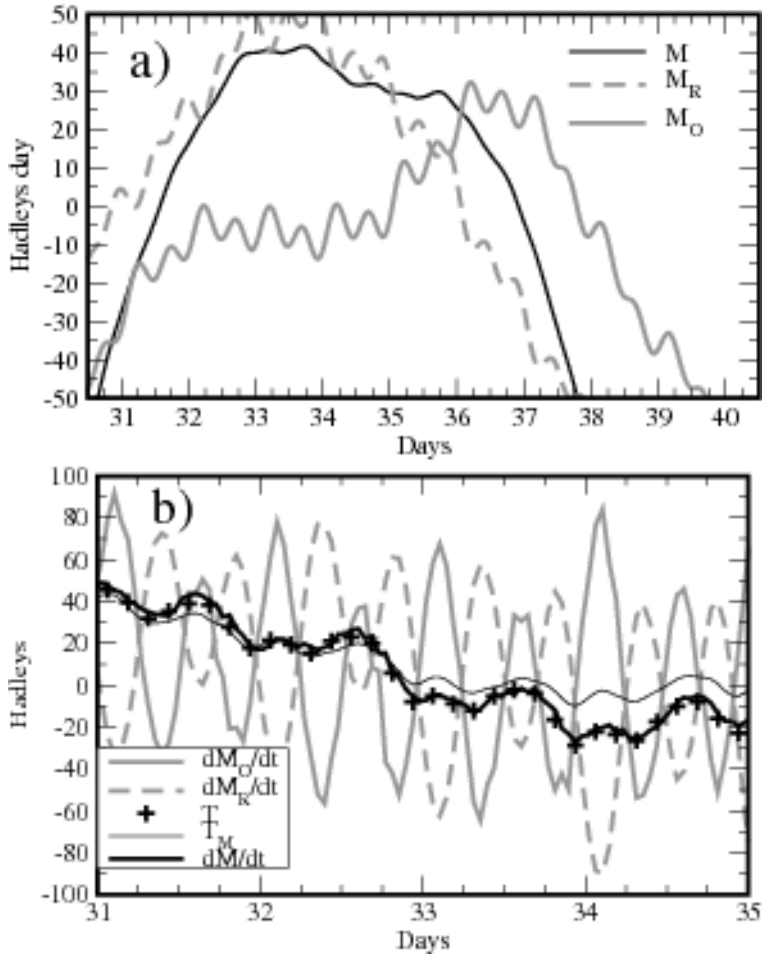
Figure 1: AAM budget in the LMDz-GCM. a) First 10 days of February: total AAM (M black solid), mass AAM (M_O grey solid), and wind AAM (M_r grey dashed). For clarity, each curve has been shifted vertically. b) First 5 days of February: global AAM tendency (dM/dt thick black solid), mass AAM tendency (dM_O/dt grey solid), wind AAM tendency (dM_R/dt grey dashed), Total Torque (T plus), and mountain torque T_M (thin solid)
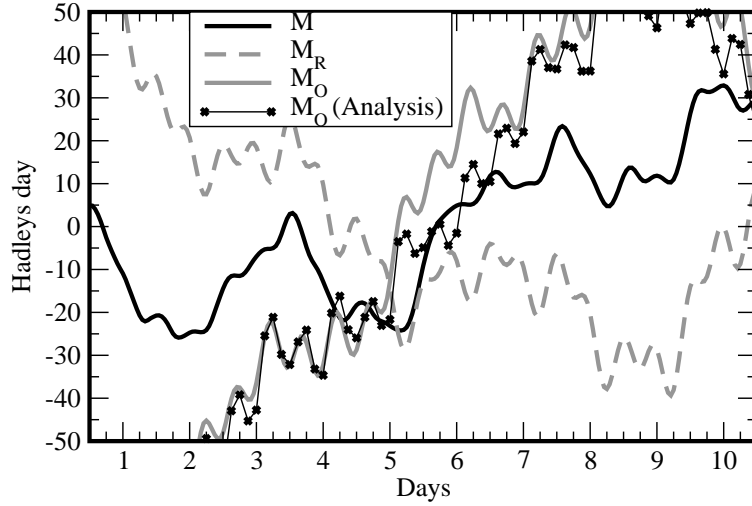
Figure 2: AAMs in the ECMWF model. 10 day forecast starting the 1 February 2004 and its corresponding analysis: total AAM (M black solid), mass AAM (M_O grey solid), and wind AAM (M_r grey dashed), mass AAM from the analysis (solid and dots). For clarity, each curve has been shifted vertically.
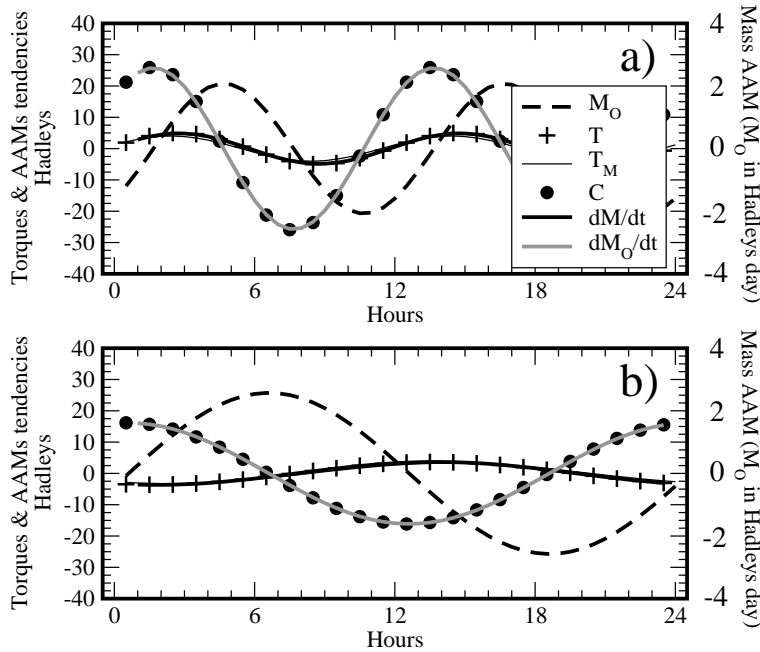
Figure 3: Mass AAM and mass AAM budgets: a) Semi-diurnal; b) Diurnal. Mass AAM (M_O thick dashed), Total torque (T plus), Mountain torque (T_M thin line), Coriolis conversion (C thick dots), Total AAM tendency (dM/dt thick solid), and mass AAM tendency (dM_O/dt thick grey). Note that in a) and b) the thin line for T_M almost coincides with the thick line for dM/dt.
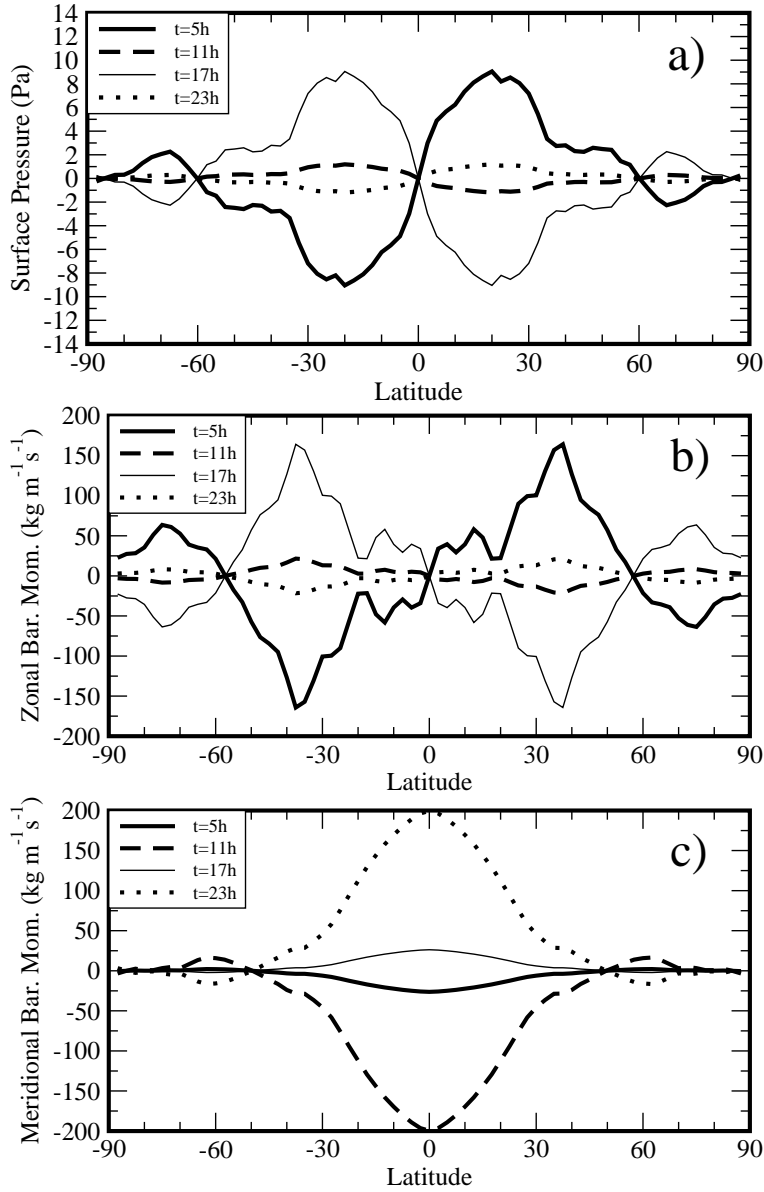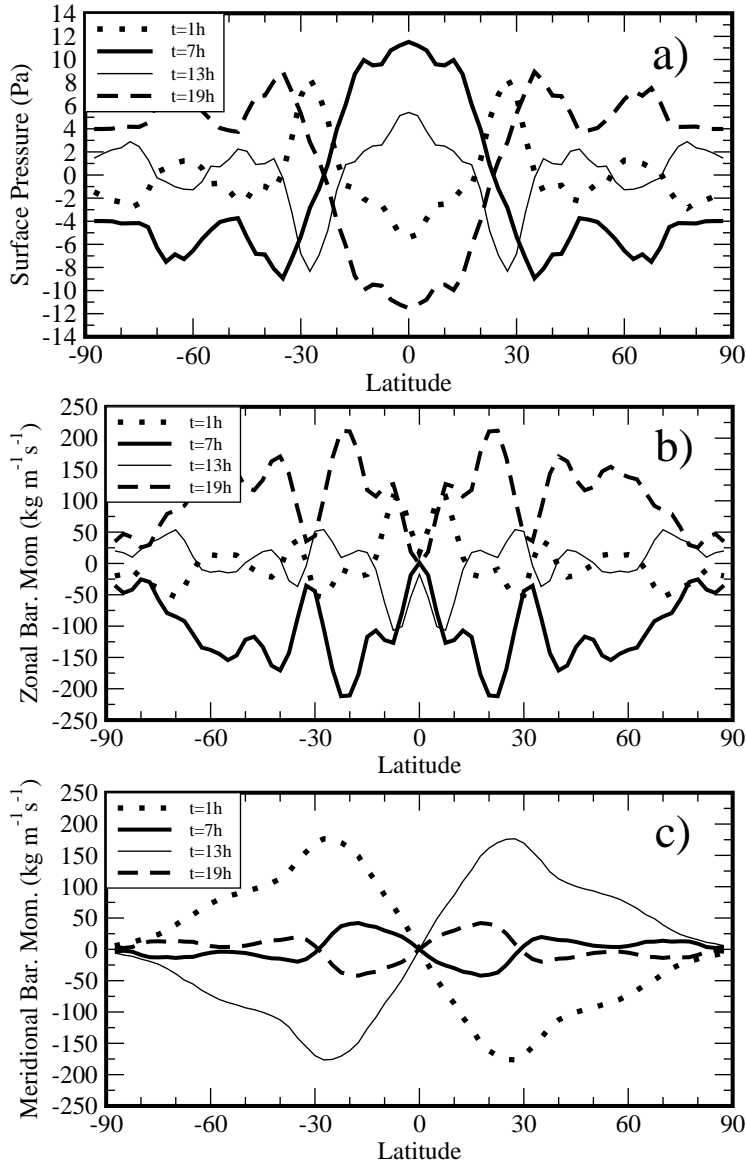
17
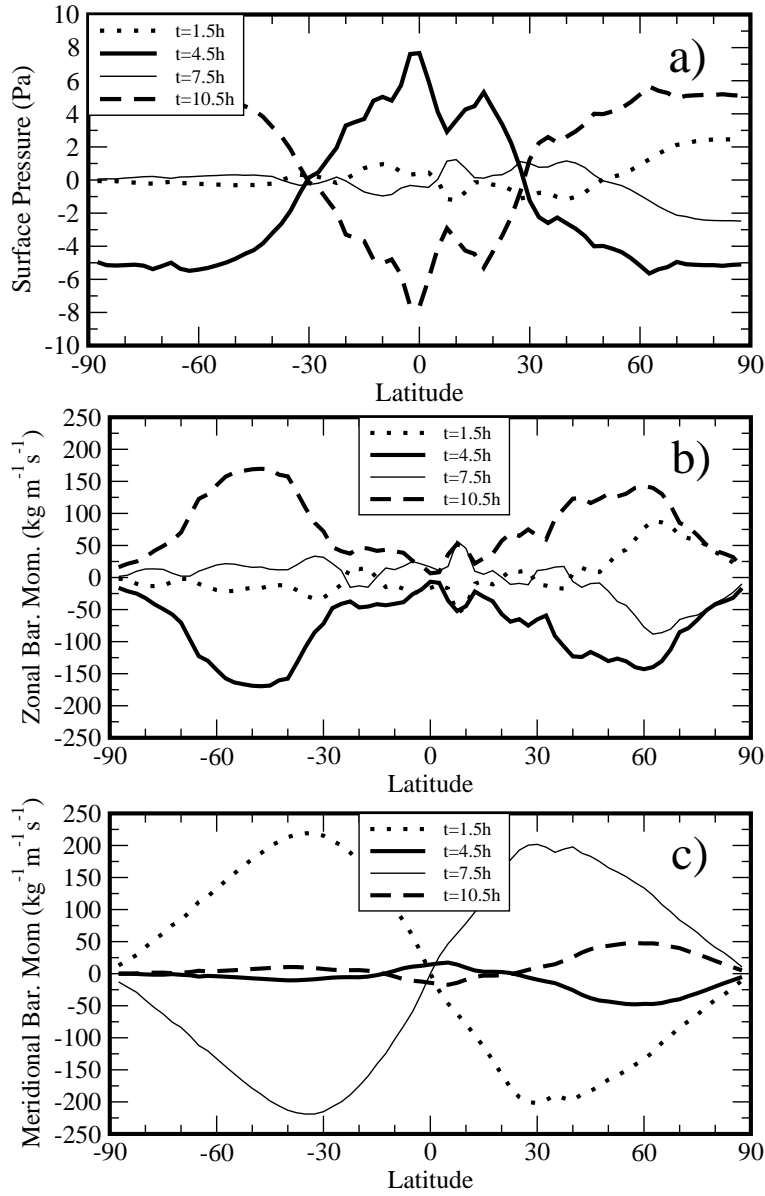
Figure 4: Semi diurnal cycle in the GCM LMDz: zonal mean and barotropic diagnostics. a) Zonal mean of the surface pressure ($g\mathcal{M}$); b) Zonal mean of the barotropic zonal momentum ($\mathcal{U}$); c) Zonal mean of the barotropic meridional momentum ($\mathcal{V}$).
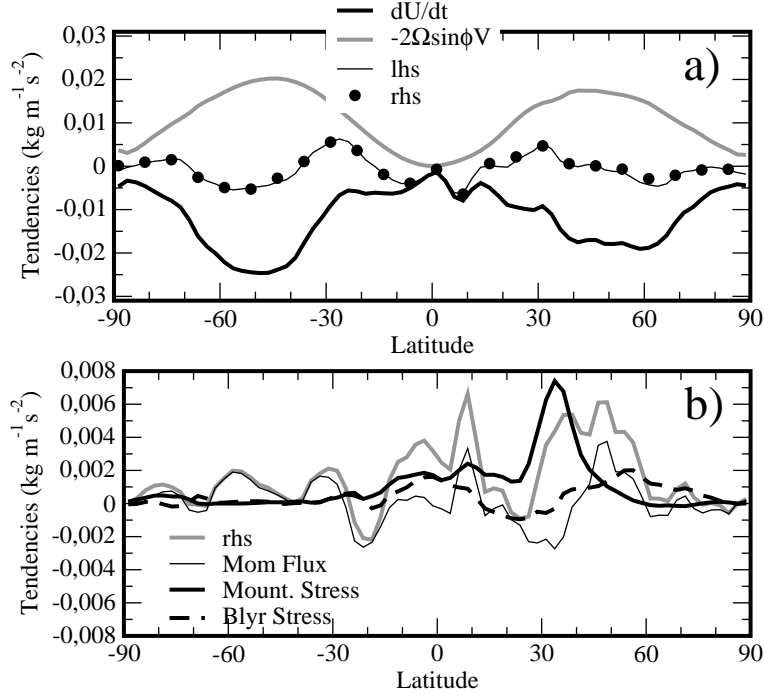
Figure 5: Zonal mean barotropic momentum budget in Eqs 1-2, semi-diurnal signals. a) t=1.5hr, zonal momentum tendency ($\partial_t \mathcal{U}$ thick solid), Coriolis term ($-2\Omega \sin\phi\mathcal{V}$ thick grey solid), RHS of Eq. 1 (thin), and LHS of Eq. 1 (dots); b) t=2.5hr, RHS of Eq. 1 (thick grey solid), momentum flux divergence ($\mathcal{F}$, thin solid), mountain stress ($\mathcal{T}$, thick black), and boundary layer stress ($\mathcal{B}$ thick black dashed).

Figure 6: Diurnal cycle in the GCM LMDz: zonal mean and barotropic diagnostics. a) Zonal mean of the surface pressure $(g\mathcal{M})$, pattern antisymmetric with respect to the Equator; b) Zonal mean of the barotropic zonal momentum $(\mathcal{U})$, pattern antisymmetric with respect to the Equator; c) Zonal mean of the barotropic meridional momentum $(\mathcal{V})$, pattern symmetric with respect to the Equator.

Figure 7: Diurnal cycle in the GCM LMDz: zonal mean and barotropic diagnostics. a) Zonal mean of the surface pressure ($g\mathcal{M}$), pattern symmetric with respect to the Equator; b) Zonal mean of the barotropic zonal momentum ($\mathcal{U}$), pattern symmetric with respect to the Equator; c) Zonal mean of the barotropic meridional momentum ($\mathcal{V}$), pattern antisymmetric with respect to the Equator.

21
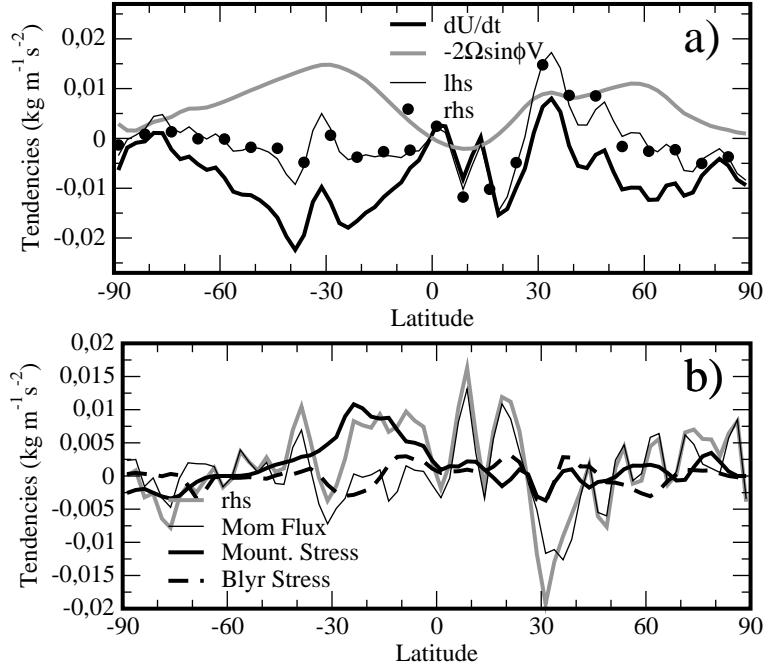
Figure 8: Zonal mean barotropic momentum budget in Eqs 1-2, diurnal signals. a) t=1hr, zonal momentum tendency ($\partial_t \mathcal{U}$ thick solid), Coriolis term (-$2\Omega \sin \phi \mathcal{V}$ thick grey solid), RHS of Eq. 1 (thin), and LHS of Eq. 1 (dots); b) t=13hr, RHS of Eq. 1 (thick grey solid), momentum flux divergence ($\mathcal{F}$, thin solid), mountain stress ($\mathcal{T}$, thick black), and boundary layer stress ($\mathcal{B}$ thick black dashed).
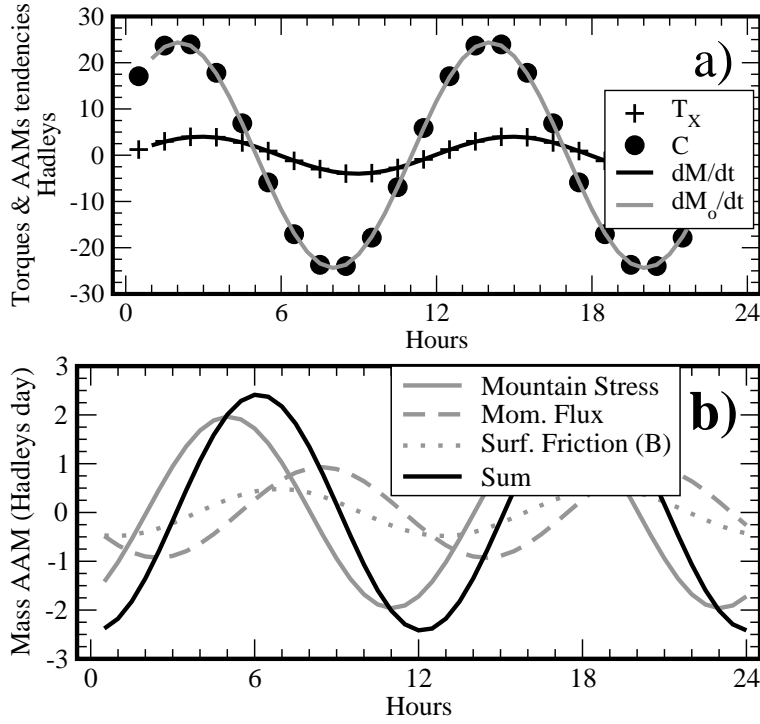
Figure 9: Semi-diurnal responses in the shallow water model with $H_0 = 9.5$km. a) AAM budget when the forcing $\tilde{X}$ is keyed to the mountain stress $\mathcal{T}$: total AAM tendency ($\frac{dM}{dt}$ thick solid), mass AAM tendency ($\frac{dM}{dt}$ thick grey solid), torque due to the the forcing (T_X plus), Coriolis conversion term (C dots), b) Mass AAM cycle when $\tilde{X}$ is keyed to the various stresses in Fig. 5a: mountain stress ($\mathcal{T}$ thick grey), momentum flux divergence ($\mathcal{F}$ thick grey dashed), boundary layer stress ($\mathcal{B}$ thick grey dots), sum ($\mathcal{T} + \mathcal{F} + \mathcal{B}$ thick black solid).
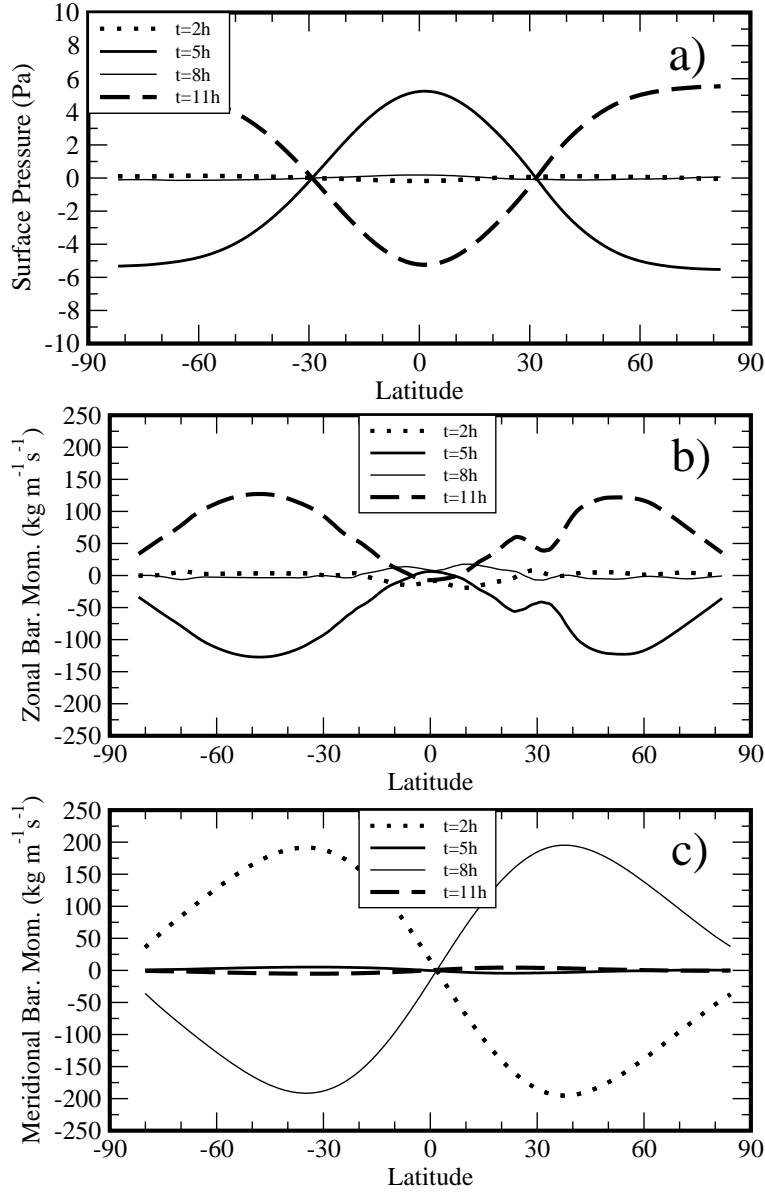
Figure 10: Semi-diurnal responses in the shallow water model with $H_0 = 9.5$km and when $\tilde{X}$ is keyed to the mountain stress $\mathcal{T}$: a) Surface Pressure (i.e. $\rho_r g \tilde{h}$); b) Zonal momentum (i.e. $\rho_r H_0 \tilde{u}$), c) Meridional momentum (i.e. $\rho_r H_0 \tilde{v}$).
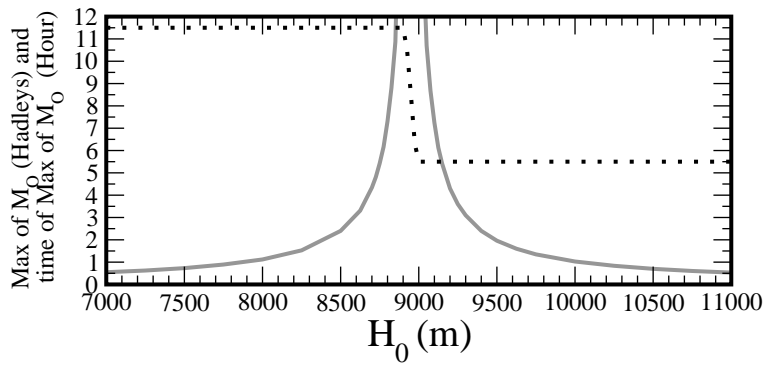
24

Figure 11: Semi-diurnal mass AAM response in the shallow water model when $\tilde{X}$ is keyed to the mountain stress $\mathcal{T}$. Sensitivity of M_O to the value of the equivalent depth H_0: amplitude of M_O (thick grey), phase of M_O (dots).
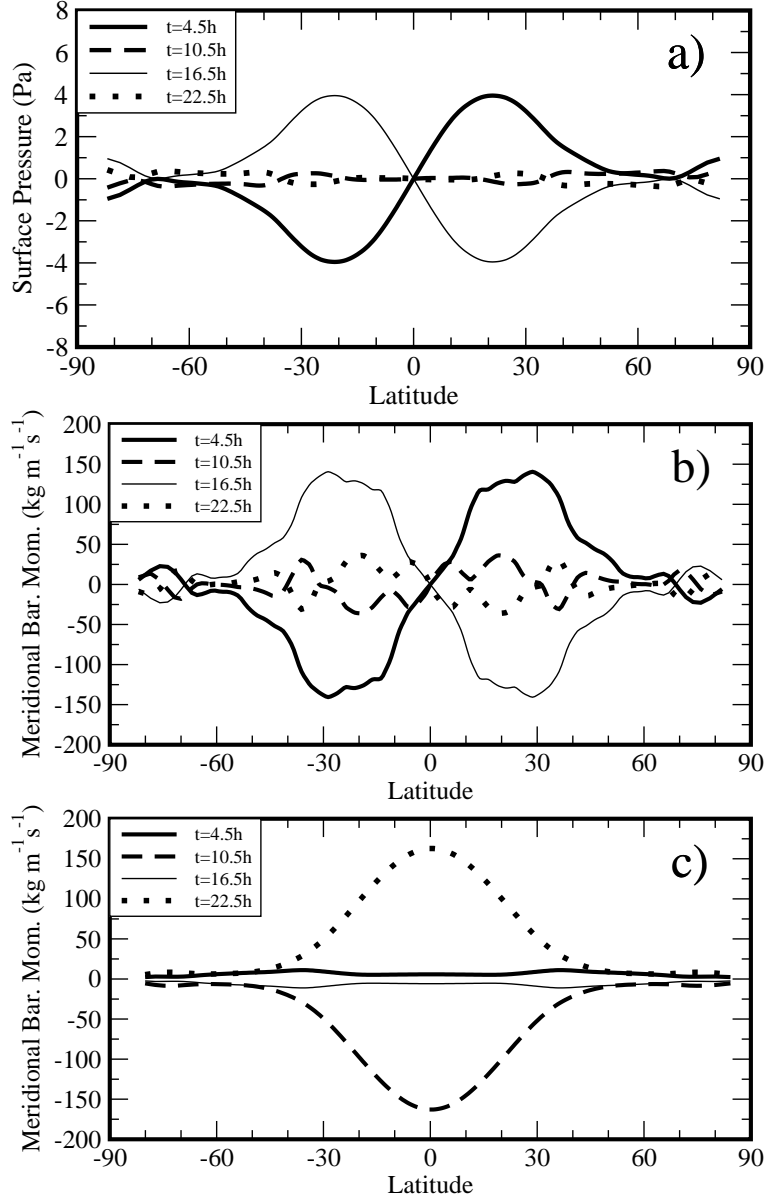
Figure 12: Diurnal response in the shallow water model with $H_0 = 2.5$km and when the forcing $\tilde{X}$ is keyed to the mountain stress $\mathcal{T}$: a) Surface Pressure (i.e. $\rho_r g\tilde{h}$) pattern antisymmetric with respect to the Equator; b) Zonal momentum (i.e. $\rho_r \frac{H_0}{2\kappa}\tilde{u}$) pattern antisymmetric with respect to the Equator; c) Meridional momentum (i.e. $\rho_r \frac{H_0}{2\kappa}\tilde{v}$) pattern symmetric with respect to the Equator.
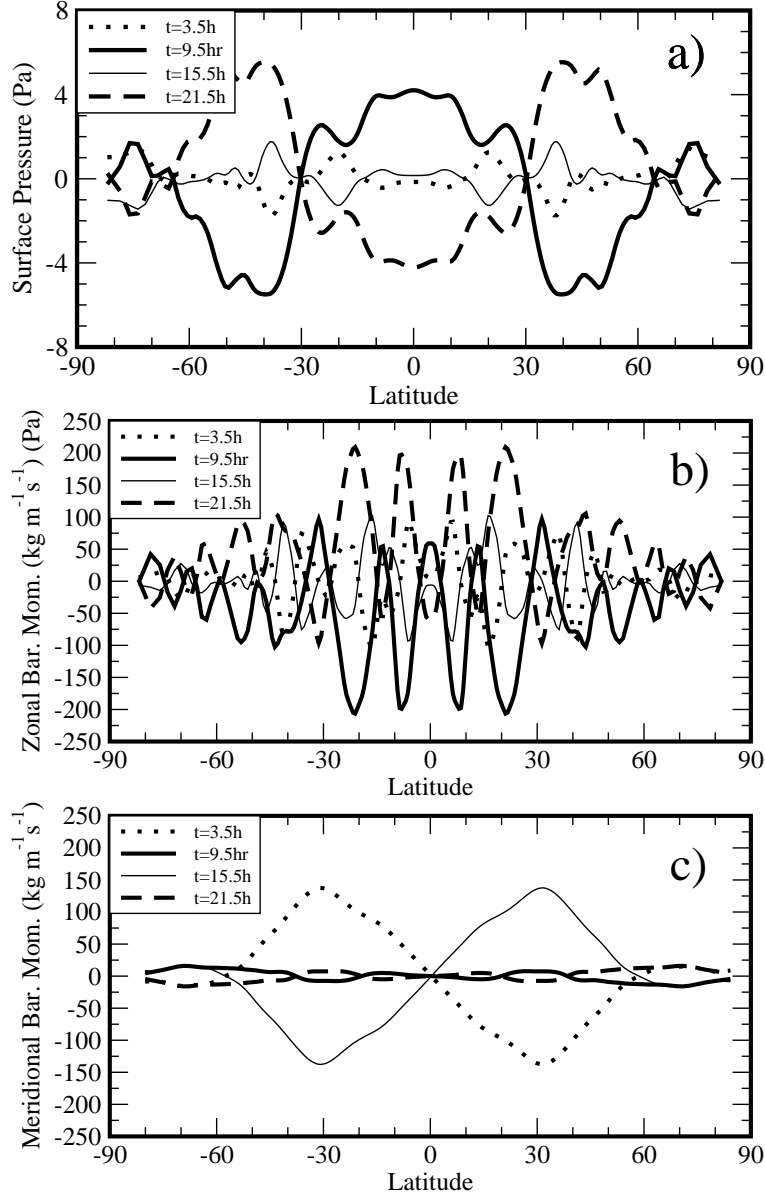
Figure 13: Diurnal response in the shallow water model with $H_0 = 1$km and when the forcing $\tilde{X}$ is keyed to the momentum flux divergence $\mathcal{F}$: a) Surface Pressure (i.e. $\rho_r g \tilde{h}$) pattern symmetric with respect to the Equator; b) Zonal momentum (i.e. $\rho_r \frac{H_0}{2\kappa} \tilde{u}$) pattern symmetric with respect to the Equator; c) Meridional momentum (i.e. $\rho_r \frac{H_0}{2\kappa} \tilde{v}$) pattern antisymmetric with respect to the Equator.
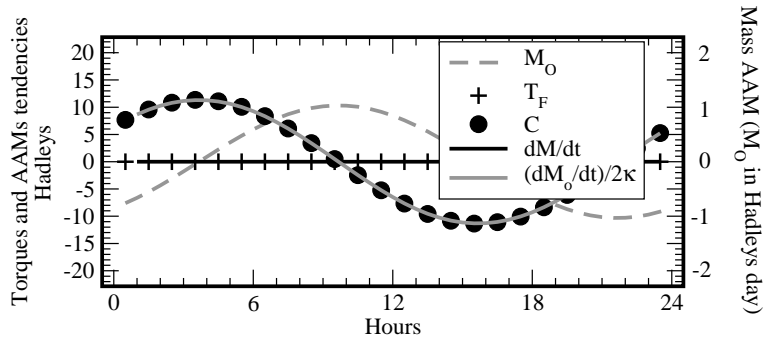
Figure 14: Diurnal response in the shallow water model with $H_0 = 1$km and when the forcing $\tilde{X}$ is keyed to the momentum flux divergence $\mathcal{F}$. Mass AAM budget: Mass AAM (grey solid), total AAM tendency ($dM/dt = 0$, black solid), mass AAM tendency (here $dM_O/dt/2\kappa$, grey solid), Mountain torque ($T_F = 0$, plus), and Coriolis conversion (C, dots).